Advances in
Geo-Energy Research

Vol. 8, No. 3, p. 193-205, 2023

Original article

A semianalytical model of fractured horizontal well with hydraulic fracture network in shale gas reservoir for pressure transient analysis

Qianchen Cui[1], Yulong Zhao[1]*, Liehui Zhang[1], Man Chen[2], Shangjun Gao[2], Zhangxing Chen[3]

[1]State Key Laboratory of Oil and Gas Reservoir Geology and Exploitation, Southwest Petroleum University, Chengdu 610500, P. R. China
[2]Sichuan Changning Natural Gas Development Co., Ltd., Chengdu 610056, P. R. China
[3]Department of Chemical and Petroleum Engineering, University of Calgary, Calgary T2N 1N4, Canada

Keywords:
Pressure transient analysis
hydraulic fracture network
multi-fractured horizontal well
shale gas
semianalytical model

Cited as:
Cui, Q., Zhao, Y., Zhang, L., Chen, M., Gao, S., Chen, Z. A semianalytical model of fractured horizontal well with hydraulic fracture network in shale gas reservoir for pressure transient analysis. Advances in Geo-Energy Research, 2023, 8(3): 193-205.
https://doi.org/10.46690/ager.2023.06.06

Abstract:
Accurate construction of a seepage model for a multifractured horizontal well in a shale gas reservoir is essential to realizing the forecast of gas well production, the pressure transient analysis, and the inversion of the postfracturing parameters. This study introduces a method for determining the fracture control region to characterize the flow area of the matrix within the hydraulic fracture network, distinguishing the differences in the flow range of the matrix system between the internal and external regions caused by the hydraulic fracture network structure. The corresponding derivation and solution methods of the semi-analytical seepage model for fractured shale gas well are provided, followed by the application of case studies, model validation, and sensitivity analysis of parameters. The results indicate that the proposed model yields computational results that closely align with numerical simulations. It is observed that disregarding the differentiation of matrix flow area between the internal and external regions of the fracture network led to an overestimation of the estimated ultimate recovery, and the boundary-controlled flow period in typical well testing curves will appear earlier. Because hydraulic fracture conductivity can be influenced by multiple factors simultaneously, conducting a sensitivity analysis using combined parameters could lead to inaccurate results in the inversion of fracture parameters.

1. Introduction

Under the current global consensus of promoting the green economy, it is difficult for the current supply of natural gas obtained from conventional reservoirs to meet continuously growing demand. As a result, attention has turned toward shale gas development (Miao et al., 2022). Shale is a fine-grained sedimentary rock that has ultra-low porosity and permeability, which leads to commercially developed shale gas reservoirs being highly dependent on the technology of multifractured horizontal well (MFHW) (Holditch, 2003; Clarkson et al., 2012). A rapid decline in production of single MFHW in shale is inevitable, and new wells must be put into production continuously to maintain sufficient reservoir operations. Thus, it is essential to evaluate the effect and economy of each MFHW (Hazlett et al., 2021). Specifically, it is necessary to use observable production data to obtain the parameters of hydraulic fracture, identify the physical properties of the shale gas reservoir, and predict the estimated ultimate recovery (EUR). This information usually can be obtained using pressure transient analysis (PTA) (Afagwu et al., 2020; Nguyen et al., 2020).

Applying a reasonable seepage model of MFHW in shale gas reservoirs provides the basis for improving the reliability of PTA interpretation results. The construction of the seepage model presents significant challenges, however, because of the multiscale pore structure in the shale rock (Moghanloo

---

*Corresponding author.
E-mail address: qianchencui@163.com (Q. Cui); swpuzhao@swpu.edu.cn (Y. Zhao); zhangliehui@vip.163.com (L. Zhang); chen-man0@petrochina.com.cn (M. Chen); hxs_800041@petrochina.com.cn (S. Gao); zhachen@ucalgary.ca (Z. Chen).
Yandy Scientific Press

2207-9963
Received May 10, 2023; revised May 30, 2023; accepted June 15, 2023; available online June 18, 2023.

Table 1. Characteristics of PTA models based on different solution methods.

Model	Advantages	Disadvantages
Analytical	Fast computational speed. Generally able to obtain high-precision solutions.	Difficult to consider complex nonlinear flow mechanisms. Unable to consider irregular fracture geometries. Difficult to consider interfracture pressure interference effects.
Semianalytical	Maintains analytical function properties and supports irregular fracture geometries.	Dense coefficient matrix, leading to potential ill-conditioning issues.
Numerical	Able to consider complex nonlinear flow mechanisms. Able to consider complex hydraulic fracture geometries.	Computationally time-consuming. Errors introduced by spatial discretization of governing equations.

and Javadpour, 2014; Tian et al., 2018; Wanget et al., 2020), the particularity of occurrence and diffusion mechanism of adsorbed shale gas, and the complex morphology of hydraulic fracture caused by large-scale hydraulic fracturing (Waltman, 2005; Daniels et al., 2007).

According to the solving methods, the PTA model of MFHW can be categorized as an analytical model, a numerical model, or a semianalytical model (Wang et al., 2019; Zhao and Du, 2019). Each method has its own characteristics, as shown in Table 1. The analytical model has been applied in PTA and RTA for vertical wells in early studies (El-Banbi and Wattenbarger, 1998; Wattenbarger et al., 1998), and consequently has been extended for use in MFHW. In the analytical PTA model of MFHW, each adjacent hydraulic fracture of MFHW is equidistant and symmetrical along the horizontal well, thus dividing the hydraulic-matrix system into multiple independent flow regions, and assuming linear fluid flow in each region. In recent decades, many scholars have proposed analytical PTA models of MFHW, and these models have focused on the principle of division of stimulated reservoir volume (SRV). In the trilinear flow model (Ozkan et al., 2009; Brown et al., 2011), for example, the region between adjacent hydraulic fractures is regarded as the SRV, and the region outside the tips of the hydraulic fracture (HF) is seen as the unstimulated reservoir volume. Based on the trilinear flow model, Stalgorova and Matter (2013) proposed five-region flow model, which assume that SRV and unstimulated reservoir volume existed between adjacent fractures, and the seepage of the ”hydraulic fracture-matrix” system could be decomposed into five regional linear flows. The analytical PTA model is widely used due to its fast calculation speed and simple model construction.

However, the analytical PTA model is not suitable for cases in which the shape of the hydraulic fracture is complex or when the pressure interference between hydraulic fractures should not be neglected. In particular, for the MFHW in reservoirs with preexisting rock-fabric heterogeneity, like shales, the hydraulic fracture easily has complex growth and forms a network during the hydraulic fracturing operation (Fisher et al., 2002; Palmer, 2007; Cipolla et al., 2010); consequently, using the analytical model for the PTA of MFHW is too idealistic.

Numerical simulation using an unstructured grid system can be used to determine the PTA of MFHW, considering the complex morphology and interference of hydraulic fractures (Wang et al., 2021; Zhang et al., 2022). Nevertheless, establishing a numerical PTA model can be difficult and time-consuming. In contrast, a more advanced approach for PTA is to use the semianalytical model (Gringarten and Ramey, 1973; Yao et al., 2013; Zhao et al., 2014; Zhao and Du, 2019; Chu et al., 2023). Many scholars have proposed the use of semianalytical models for MFHW to consider the various characteristics of hydraulic fractures, including hydraulic fractures with unequal length (Zhao et al., 2016), different directions of the fracture extension (Wang, 2014), and the complex shape of reservoir boundary (Zhao et al., 2017). In addition, some researchers have considered an important case of MFHW, that is, hydraulic fractures form a hydraulic fracture network (HFN). Some studies have applied the fractal theory to characterize the HFN (Fan and Ettehadtavakkol, 2017; Zhang and Yang, 2021). In these models, however, the morphology of hydraulic fracture is just tree-like branching but is not in the network. In contrast, some of the models proposed by other scholars better reflect the network shape of hydraulic fractures: For example, Jia et al. (2015) constructed a semianalytical model of MFHW with HFN, which applied the star-delta transformation method (Karimi-Fard et al., 2004) to deal with the flow relations of intersecting fractures in a complex fracture network. They further investigated the complex shape of the SRV boundary by combining the boundary element method (Jia et al., 2017). Ren et al. (2019) developed a well-pattern model considering complex HFN and analyzed the sensitivity of fracture-related parameters. Chen et al. (2017, 2018) developed a semianalytical model to consider arbitrarily distributed fractures.

An important phenomenon in the existing semianalytical PTA model of MFHW with HFN has not been address, that is, the HFN divides the SRV region into two parts: one is surrounded by hydraulic fractures, which is located on the inside region of the fracture network (IFNR), and the other is located on the outside region of the fracture network (OFNR), as shown in Fig. 1(a). During the production period, under the effect of production pressure difference, the gas in the matrix will flow into the hydraulic fracture. With the gradual expansion of the pressure drop area, the flow area increases. The shale matrix in the OFNR is usually homogeneous with

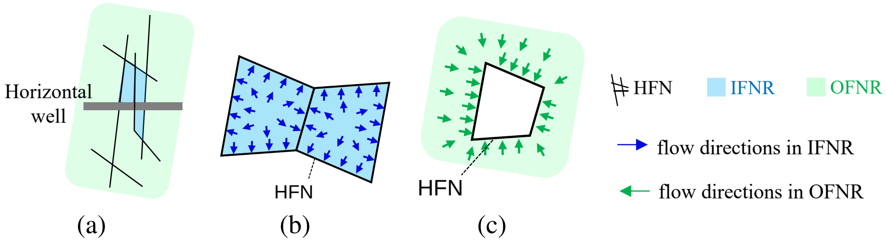

Fig. 1. The sketch map of a simplified HFN-matrix system. (a) The sketch of horizontal well with HFN, (b) gas flow directions of the IFNR matrix and (c) gas flow directions of the OFNR matrix.

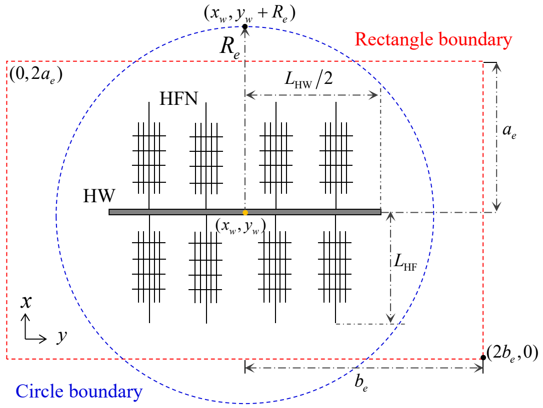

Fig. 2. Structure diagram of the physical model of MFHW with HFN in shale gas reservoir.

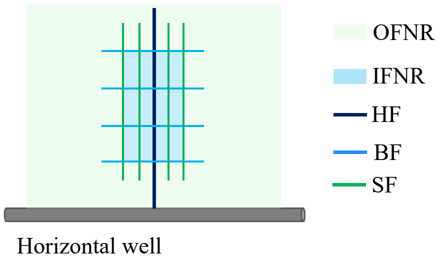

Fig. 3. Schematic of a single wing of HFN.

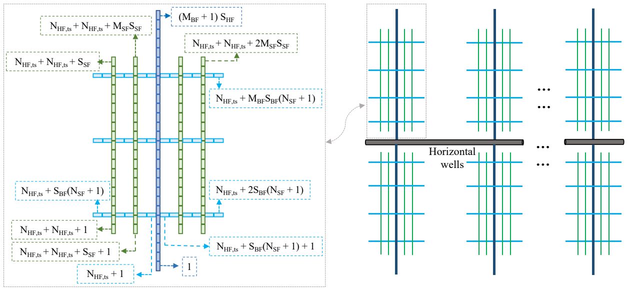

Fig. 4. Schematic of discrete fracture network elements.

the petrol-physical properties, and it has the same outer seepage boundary, therefore, the OFNR could be considered as a continuous pressure system. Conversely, the IFNR matrix did not have an external fluid supplement because of the hydraulic fracture shielding, which also made the outer seepage boundary of the matrix in the IFNR different from that of the OFNR. No fluid was exchanged between the IFNR elements or between the IFNR and the OFNR (as shown in Figs. 1(b) and 1(c)). The existing semianalytical PTA model for MFHW with HFN does not consider the differences in the seepage boundary between the IFNR and OFNR matrix.

In light of this, this study developed a semianalytical model of the MFHW with HFN in shale gas reservoirs. The primary improvement of this model is its ability to divide the SRV region into the IFNR and the OFNR. In addition, a boundary of the fracture-controlled region (FCR) was proposed to characterize the outer seepage boundary of the IFNR matrix. The typical curves were drawn to denote the division of the flow stages in our model, and verified the model according to a numerical model. Finally, using our model and a numerical simulator, assessed the influence of the differences in the seepage boundaries between the IFNR and the OFNR on the typical curve and production rate, and analyzed the effects of some of the model parameters on the type curve.

2. Physical model

2.1 Structure of the MFHW with HFN and shale matrix system

The physical structure of the MFHW with the HFN model is shown in Fig. 2. The model assumes that the reservoir boundaries are no-flow, and there are two geometries are considered: Circular and rectangular. In the case of a circular reservoir, the radius of the circular boundary is denoted as R_e, and the circular reservoir is located at the midpoint (x_w, y_w) of a horizontal well. For the rectangular reservoir, the half-length of the long axis is denoted as b_e, and the half-length of the short axis is denoted as a_e. In addition, the length of the horizontal well was L_{HW} and the half-length of the single HFN group was L_{HF}.

2.2 HFN system

The structure of the HFN in our model is assumed to be an orthogonal rectangular network, as shown in Fig. 3. This study decomposed the HFN into three types of hydraulic fractures: The primary HF, which was connected to the horizontal well; the branch fracture (BF), which intersected with the HF but was not connected directly to the wellbore; and the secondary fracture (SF), which communicated with the BF.

All segments of the HFN need to be reasonably ordered to facilitate the construction of the model solution. The ordering rules of each discrete fracture segment are shown in Fig. 4,

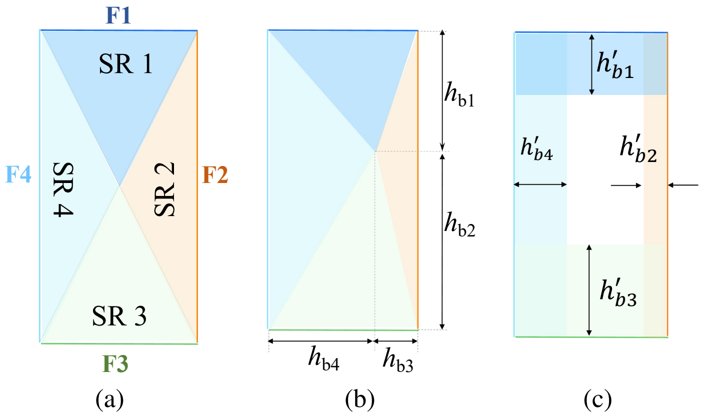

(a) (b) (c)

Fig. 5. Illustration of FCR division method to characterize the outer seepage boundary of matrix in IFNR.

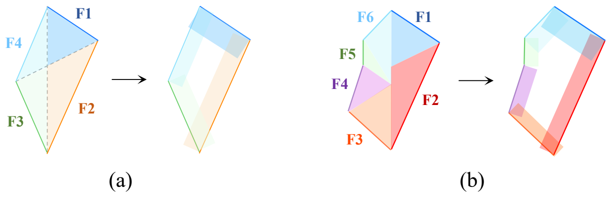

(a) (b)

Fig. 6. IFNR element and splitting supply area for the complex HFN. (a) Quadrilateral HFN and (b) polygonal HFN.

where M_{BF} is the number of BF intersecting with a single wing of HF; M_{SF} is the number of SF at one side of a single HF wing; S_{HF} is the number of discrete segments of HF; S_{BF} is the number of discrete segments of a single half of BF; and S_{SF} is the number of discrete segments of a single SF. The discrete HFN elements are sorted in the order of HF-BF-SF (e.g., the index of the first discrete element of BF is $N_{t,HN}$ + 1, and the index of the first discrete element of SF is $N_{t,HF}$ + $N_{t,BF}$ + $N_{t,SF}$ + 1). The number of totally fracture network segment $N_{t,FN}$ is as follows:

$$N_{t,FN} = \sum N_{t,\Omega} = 2M_{HF}\left[S_{HF} + 2\left(M_{SF}+1\right)S_{BF} + 2M_{SF}S_{SF}\right], \quad (\Omega = \mathrm{HF}, \mathrm{BF}, \mathrm{SF}) \tag{1}$$

where M_{HF} is the number of HF.

2.3 The FCR and outer seepage boundary of matrix in IFNR

The concept of using FCR to characterize the outer seepage boundary of the IFNR matrix was mentioned before, and the FCR represents the spectrum of effects associated with the pressure drop, which a fracture can cause. Because the IFNR is a closed region and each fracture that forms the IFNR has its own FCR, the fluid in the matrix within these FCRs flows independently, and this fluid is supplied to the fracture section connected to them only. As a result, for the IFNR, the FCR boundary provides a means to characterize the outer boundary of matrix seepage.

As shown in Fig. 5(a), for instance, a rectangular IFNR unit is composed of four fracture segments (represented by F1-F4), and the matrix region is divided into four FCRs, labeled Sub-region1 to Sub-region4. Because the feature parameters of these fractures, such as permeability, width, and length, may be different, the division of the FCR area in the IFNR needs to match the flow capacity of the fracture—that is, the higher the seepage capacity of the fracture, the larger the area of its FCR will be (as shown in Fig. 5(b)). A weighted average method was subsequently applied to ensure that the ratio of each FCR area corresponds to the ratio of the feature parameters, as shown below:

$$\beta_i = \frac{A_{c,i}}{\sum_{i=1}^{4}\left(A_{c,i}\right)} = \frac{l_{Fi}w_{Fi}k_{Fi}}{\sum_{i=1}^{4}\left(l_F w_F k_F\right)_i} \tag{2}$$

where β_i is the area proportion of the i-th FCR, constant; $A_{c,i}$ is the area of the i-th FCR, m^2; l_{Fi} indicates the length of i-th hydraulic fracture, m; w_{Fi} indicates the width of i-th hydraulic fracture, m; k_{Fi} indicates the permeability of i-th hydraulic fracture, m^2.

The area determined by Eq. (2) represents the control volume of each hydraulic fracture segment over the shale matrix. However, the boundaries of this region need to be redefined to facilitate solving the seepage equations. To achieve this, while ensuring equal area or constant control volume, assuming each FCR region of each hydraulic fracture segment was assumed to be a rectangle, as shown Fig. 5(c), with the fracture segment as the long side and the height as the distance to the flow boundary. This is calculated using the following equation:

$$h'_{c,i} = \frac{A_{c,i}}{l_{Fi}} \tag{3}$$

where $h'_{c,i}$ is the apparent outer seepage boundary of matrix in i-th FCR.

The pseudo-no-flow boundaries for each FCR were determined by applying Eqs. (2)-(3), which resulted in boundaries parallel to their connected fractures. The boundary condition for the IFNR matrix can be expressed as follows:

$$\left.\frac{\partial p}{\partial \xi_y}\right|_{\xi_y = h'_{c,i}} = 0 \tag{4}$$

where p indicates the reservoir pressure of IFNR, Pa; the ξ_y represents the distance between the any point and the boundary of i-th apparent FCR, m.

In addition, the previous FCR-boundary method is suitable for the irregular quadrilateral and polygonal shapes of complex HFN, as shown in Fig. 6.

3. Mathematical model and solution

The assumptions of our model are as follows: (1) The effects of gravity and capillary force are negligible; (2) consider isothermal infiltration; (3) the gas desorption expression by the Langmuir isotherm equation; (4) the tips of hydraulic fracture seemed as a no-flow boundary; (5) The reservoir boundary is no-flow and is depicted with a circle or rectangle; and (6) the shale matrix is described using the De Swaan model.

3.1 The governing equations of gas flow

3.1.1 Governing equations of gas flow in the shale matrix

According to the approach taken by Ozkan et al. (2010), the motion equation of gas in shale matrix porosity can be described as follows:

$$\begin{cases} v_m = \frac{k_{ma}}{\mu_g}\frac{\partial p_m}{\partial r} \\ k_{ma} = \frac{k_m}{\mu_g}\left(1+\frac{\mu_g c_g D_g}{k_m}\right) \end{cases} \tag{5}$$

where v_m indicates gas velocity, m/s; k_{ma} is the apparent permeability of shale matrix, considering the Knudsen diffusion effect, m^2; p_m is the pressure of matrix pore, Pa; μ_g is the gas viscosity, Pa·s; k_m is the shale matrix permeability, m^2; c_g is gas compressibility, Pa^{-1}; D_g is the diffusivity constant, m^2/s; r is the distance, m.

Applying the method proposed by Ertekin et al. (1986), the diffusivity constant D_g, was calculated as follows:

$$D_g = \frac{3.405\times10^{-8}}{\sqrt{M_g}}k^{0.67} \tag{6}$$

The diffusion equation of gas flow in the shale matrix is given as follows:

$$\frac{1}{r_m^2}\frac{\partial}{\partial r_m}\left(r_m^2 k_m \frac{p_m}{\mu_g z}\frac{\partial p_m}{\partial r_m}\right)+\frac{RT}{M_g}q_m^* = \phi_m\frac{\partial}{\partial t}\left(\frac{p_m}{z}\right) \tag{7}$$

where r_m indicates Radial distance between point and sphere center, m; z is the compressibility factor, dimensionless; ϕ_m is the porosity of the shale matrix, constant; M_g is the average molecular weight, kg/mol; R is the universal gas constant, $R = 8.314$ J/(mol·K); T is formation temperature, K; q_m^* is the diffusion rate of desorption gas, m^3/s; t is time, s.

According to the Langmuir isotherm equation, the q_m^* in Eq. (7) can be written as follows:

$$q_m^* = -\frac{M_g p_{sc}}{RT_{sc}}\left(1-\phi_m-f_f\right)\frac{V_L p_L}{\left(p_L+p_m\right)^2}\frac{\partial p_m}{\partial t} \tag{8}$$

where p_{sc} is the pressure under standard condition, Pa; T_{sc} is the temperature under standard condition, K; f_f is proportion of micro-fracture volume in unit volume rock, dimensionless; V_L is the Langmuir volume, sm^3/m^3; p_L is the Langmuir pressure, Pa.

Using the gas pseudo-pressure to linearize the gas seepage function, can define the follows:

$$m_\chi = 2\int_0^{p_\chi}\frac{p}{\mu(p)z(p)}\mathrm{d}p; \quad (\chi = m,f,F) \tag{9}$$

where m_χ is pseudo-pressure, Pa/s; the subscripts m, f and F indicate matrix, microfracture, and hydraulic fracture, respectively.

Substituting Eq. (9) into Eqs. (7)-(8), yields the following:

$$\begin{cases} \frac{\partial^2 m_m}{\partial r^2} = \frac{\phi_m\mu_g\bar{c}_{tm}}{k_m}\frac{\partial m_m}{\partial t} \\ \bar{c}_{tm} = \left[\frac{2p_{sc}T}{T_{sc}}\left(1-\phi_m-f_f\right)\frac{V_L p_L \mu_g z}{(p_L+p_m)^2 p_m}+\frac{\phi_m\mu_g c_{tm}}{k_m}\right] \end{cases} \tag{10}$$

where $\bar{c}_{tm}$ indicates the apparent total compressibility of matrix, Pa^{-1}; c_{tm} is the total compressibility, Pa^{-1}, $c_{tm} = c_m + c_g$.

The diffusive gas flowed from the interior of the matrix particle to the surface is spherical symmetry; thus, the internal boundary condition is:

$$\lim_{r_m\to0}\left(r_m^2\frac{\partial m_m}{\partial r_m}\right) = 0 \tag{11}$$

the external boundary condition is:

$$m_m|_{r_m=R_m} = m_f(r,t) \tag{12}$$

where R_m indicates the matrix particle radius, m; and the initial condition is:

$$m_m\left(r_m, t=0\right) = m_i \tag{13}$$

where m_i indicates the initial pseudo-pressure of the reservoir, Pa/s.

The following equation gives the diffusion equation for gas flow in the microfracture based on the assumption of the shale matrix physical model:

$$\nabla^2 m_f + 2\frac{RT}{M_g}\frac{1}{k_f}\tilde{q}_m\left(R_m,t\right) = \frac{\phi_f\mu_g c_{tf}}{k_f}\frac{\partial m_f}{\partial t} \tag{14}$$

where the c_{tf} is the compressibility of microfractures, Pa^{-1}; k_f indicates the micro-fracture permeability, m^2; ϕ_f indicates the micro-fracture porosity, constant; the c_{tf} indicates the total compressibility of micro-fracture, Pa^{-1}; $\tilde{q}_m$ is the mass flow rate intensity (or mass flux per unit length) of gas from the matrix to micro-fracture, kg/(m^3·s), which can be written as follows:

$$\tilde{q}_m\left(R_m,t\right) = \rho_g\frac{A_m}{V_f}v_m\left(R_m,t\right) = \rho_g\frac{\pi R_m^2}{h_f}v_m\left(R_m,t\right) \tag{15}$$

where the ρ_g indicates the gas density, kg/m^3; the h_f indicates the fracture height, m; the $\tilde{q}_m$ can be obtained according to the boundary condition of the gas flow in the spherical matrix block as follows:

$$\tilde{q}_m\left(R_m,t\right) = \frac{M_g}{RT}\frac{k_m}{h_f}\frac{\partial m_m}{\partial r_m}\bigg|_{r_m=R_m} \tag{16}$$

Substituting Eq. (16) into Eq. (14) yields the following:

$$\nabla^2 m_f + \frac{2}{h_f}\frac{k_m}{k_f}\frac{\partial m_m}{\partial r_m}\bigg|_{r_m=R_m} = \frac{\phi_f\mu_g c_{tf}}{k_f}\frac{\partial m_f}{\partial t} \tag{17}$$

The internal boundary of gas flow in microfractures is:

$$\lim_{r\to0}\frac{\pi r h_t k_f T_{sc}}{p_{sc}T}\frac{\partial m_f}{\partial r} = q_f \tag{18}$$

where the q_f is the volume rate of microfractures, m^3/s; and h_t is the reservoir thickness, m.

The outer boundary conditions of gas flow in the microfracture can be expressed as follows:

$$\lim_{r\to R_x} r\frac{\partial m_f}{\partial r}=0 \tag{19}$$

where the R_x is the boundary distance, m, $R_x=h'_{si}$ for the microfracture in the IFNR, and $R_x=R_e$ for the microfracture in OFNR.

3.1.2 Governing equations of gas flow in HFN

The seepage equation of gas flow in the hydraulic fracture is as follows:

$$\begin{cases} \frac{\partial^2 m_F}{\partial \zeta^2}+2\frac{RT}{M_g}\frac{\mu_g}{k_F}\tilde{q}_{fF}\left(\frac{w_f}{2},t\right)=\frac{1}{\eta_F}\frac{\partial m_F}{\partial t} \\ \eta_F=\frac{k_F}{\phi_F\mu_g C_{tF}} \end{cases} \tag{20}$$

where the w_f indicates the width of the micro-fracture, m; the ϕ_F indicates the hydraulic fracture porosity, constant; C_{tF} indicates total compressibility of the hydraulic fracture, Pa^{-1}; the ζ is the extension direction of hydraulic fracture, m (As shown in Fig. 2, the ζ represents the x-direction for the HF and SF, and indicates the y-direction for the BF); $\tilde{q}_{fF}$ is the crossflow rate intensity between the micro-fracture and hydraulic fracture, kg/(m^3·s), which takes the following form:

$$\tilde{q}_{fF}\left(\frac{w_F}{2},t\right)=\frac{2\rho_g}{w_F}v_f\bigg|_{r=w_F/2} \tag{21}$$

where the v_f indicates the flow velocity for gas in the micro-fractures, m/s.

Considering that the porosity and compressibility of hydraulic fracture are extremely small, the permeability of hydraulic fracture is enormous. Thus, the right hand term of Eq. (20) usually can be ignored. Substituting the Eq. (21) into Eq. (19), the Eq. (20) could be rewritten as follows:

$$\frac{\partial^2 m_F}{\partial \zeta^2}+\frac{2}{F_{CD}\zeta}\frac{\partial m_f}{\partial \delta_f}\bigg|_{v_f=w_F/2}=0 \tag{22}$$

where the F_{CD} is the dimensionless conductivity of hydraulic fracture, dimensionless; the δ indicates the normal direction of ζ, m.

3.2 Model solution

For convenience to solve seepage equation, the dimensionless rules of model parameters are used in model solving, and the Laplace transformations are used to solve the seepage partial differential equation (see Appendix A in Supplementary file for details).

3.2.1 Solution of gas flow in the matrix system

The solution of the seepage equation of the shale matrix is as follows (see Appendix B in Supplementary file for details):

$$\bar{m}_{mD}=R_{mD}\frac{\sinh\left[r_{mD}\sqrt{u_m(s)}\right]}{r_{mD}\sinh\left[R_{mD}\sqrt{u_m(s)}\right]}\bar{m}_{fD} \tag{23}$$

where $u_m(s)$ is a process variable, $u_m=s/\eta_{mD}$, and the η_{mD} indicates dimensionless pressure conductivity coefficient of the matrix, the s is Laplace variable; $\bar{m}_{mD}$ and $\bar{m}_{fD}$ respectively indicate the dimensionless pseudo pressure of mtrix and microfracture in Laplace domain; r_{mD} and R_{mD} respectively indicate dimensionless radial distance and matrix particle radius.

Under the condition of a circular closed boundary, the pressure solution for the microfracture system is as follows:

$$\bar{m}_{fD}=\bar{q}_D\ \mathrm{K}_0\left[r_D\sqrt{f_f(s)}\right] \tag{24}$$

where $\bar{q}_D$ indicates dimensionless flow rate in Laplace domain; $\mathrm{K}_0()$ indicates zeroth-order modified Bessel function; $f_f(s)$ is a process variable, its expression is provided in Eq. (B-6) of Appendix B in the supplementary files.

The Eq. (24) for the rectangle reservoir boundary condition and IFNR matrix, the solution of dimensionless pseudo-pressure of the microfracture is given in Appendix B in Supplementary file.

3.2.2 Solution of gas flow in HFN

The dimensionless equation of gas flow in the HFN according to the Laplace transformation is as follows (see Appendix C in Supplementary file for detail):

$$\bar{m}_{\Omega D}(0)-\bar{m}_{\Omega D,i}\left(\zeta_{\Omega D}\right)= \frac{2\pi}{F_{CD,i}}\left(2\bar{\tilde{q}}_{\Omega D,i}\Delta l_{FD,i}\zeta_{\Omega D,i}-\int_0^{\zeta_{\Omega D}}\int_0^{\theta_{\Omega D}}\bar{\tilde{q}}_{\Omega D,i}\mathrm{d}\theta\mathrm{d}\zeta\right) \tag{25}$$

where the subscript ω indicates HF, BF and SF; the subscript i is the index of the fracture segment number; ζ_D indicates the dimensionless distance along the fracture; F_{CD} indicates the dimensionless fracture conductivity; $\bar{\tilde{q}}_D$ indicates the dimensionless flow rate intensity in Laplace domain; Δl_D indicates the dimensionless length

The line source solution of microfractures in the OFNR within a circular closed domain is taken as an example. On the basis of the serial number of discrete HFN segments, the pressure drops at the i-th segment caused by the j-th fracture are presented as follows:

$$\bar{m}_{\Omega D,i,j}=\int_{\zeta_{mD,i}-\Delta l_{sD,i}/2}^{\zeta_{mD,i}+\Delta l_{sD,i}/2}\bar{\tilde{q}}_{\Omega D,j}\left\{K_0\left[r_D\sqrt{f_f(s)}\right]\right\}\mathrm{d}\tau \tag{26}$$

where $\zeta_{mD,i}$ is the dimensionless coordinate distance of midpoint of i-th fracture segment; $\Delta l_{sD,i}$ is dimensionless length of i-th fracture segment; r_D is as follows:

$$r_D=\sqrt{\left(\zeta_{mD,j}-\tau\right)^2+\left(\xi_{mD,j}-\omega\right)^2} \tag{27}$$

where $\left(\zeta_{mD,j},\xi_{mD,j}\right)$ indicates the dimensionless coordinate of the midpoint of j-th hydraulic fracture; (τ,ω) indicate the dimensionless coordinate for the any arbitrary point along the j-th fracture.

According to the superposition principle, the pressure response of the i-th fracture segment caused by all HFNs can be given as follows:

$$\bar{m}_{\Omega D,i}=\sum_{j=1}^{N_{t,FN}}\bar{\tilde{q}}_{\Omega D,j}\int_{\zeta_{mD,i}-\Delta l_{sD,i}/2}^{\zeta_{mD,i}+\Delta l_{sD,i}/2}\left\{K_0\left[r_D\sqrt{f_f(s)}\right]\right\}\mathrm{d}\tau \tag{28}$$

The pressure drop between the wellbore and i-th fracture segment of HF in the Laplace domain is as follows:

$$\begin{cases} \bar{m}_{wD}-\bar{m}_{HFD,i}=\dfrac{2\pi}{F_{CD,i}}S_{HF,i}^{W} \\ S_{HF,i}^{W}=\zeta_{mD,i}\displaystyle\sum_{n=1}^{S_{HF}(1+M_{BF})}\bar{\bar{q}}_{FD,n} \\ \qquad -\displaystyle\sum_{n=1}^{i-1}\left(\dfrac{\Delta\zeta_{D,n}}{2}+\Delta\zeta_{D,i}-\sum_{m=1}^{n}\Delta\zeta_{D,m}\right)\bar{\bar{q}}_{FD,n} \\ \qquad -\dfrac{(\zeta_{mD,i}-\zeta_{eD,i})^{2}}{2\Delta\zeta_{D,i}}\bar{\bar{q}}_{FD,i} \end{cases} \tag{29}$$

where the superscript W indicates wellbore, $\bar{m}_{wD}$ and $\bar{m}_{HFD,i}$ respectively indicate the dimensionless pseudo-pressure at wellbore bottom and i-th hydraulic fracture; $\Delta\zeta_{D,n}$ indicates the dimensionless relative distance; $\zeta_{mD,i}$ and $\zeta_{eD,i}$ respectively indicate the midpoint and endpoint distance of i-th hydraulic fracture.

According to the assumption of the flow sequence of HFN, if the i-th segment of the n-th BF wing crosses with the j-th segment of HF, the pressure drops between them can be expressed as follows:

$$\begin{cases} \bar{m}_{HFD,j}-\bar{m}_{BFD,i}=\dfrac{2\pi}{F_{CD,i}}S_{BF,i}^{HF,j} \\ S_{BF,i}^{HF,j}=\zeta_{mD,i}\displaystyle\sum_{v=1}^{S_{BF}(1+M_{SF})}\bar{\bar{q}}_{BFD,v} \\ \qquad -\dfrac{(\zeta_{mD,i}-\zeta_{eD,i})^{2}}{2\Delta\zeta_{D,i}}\bar{\bar{q}}_{BFD,i} \\ \qquad -\displaystyle\sum_{v=1}^{i-1}\left(\dfrac{\Delta\zeta_{D,v}}{2}+\Delta\zeta_{D,i}-\sum_{\sigma=1}^{v}\Delta\zeta_{D,\sigma}\right)\bar{\bar{q}}_{BFD,v} \end{cases} \tag{30}$$

The pressure drops between the i-th segment of BF, and the wellbore can be represented as follows:

$$\bar{m}_{WD}-\bar{m}_{BFD,i}=2\pi\left(\frac{S_{BF,i}^{HF,j}}{F_{CD,i}}+\frac{S_{HF,j}^{W}}{F_{CD,j}}\right) \tag{31}$$

For the i-th segments of the n-th SF wing, which crosses with the j-th segments of the m-th BF wing, the pressure drops between the i-th segment of BF and the j-th segments of BF can be expressed as follows:

$$\begin{cases} \bar{m}_{BFD,j}-\bar{m}_{SFD,i}=\dfrac{2\pi}{F_{CD,k}}S_{SF,i}^{BF,j} \\ S_{SF,i}^{BF,j}=\zeta_{mD,i}\displaystyle\sum_{n=1}^{S_{SF}}\bar{\bar{q}}_{SFD,i}-\dfrac{(\zeta_{mD,i}-\zeta_{eD,i})^{2}}{2\Delta\zeta_{D,i}}\bar{\bar{q}}_{SFD,i} \\ \qquad -\displaystyle\sum_{v=1}^{i-1}\left(\dfrac{\Delta\zeta_{D,n}}{2}+\Delta\zeta_{D,i}-\sum_{\sigma=1}^{v}\Delta\zeta_{D,v}\right)\bar{\bar{q}}_{SFD,v} \end{cases} \tag{32}$$

In addition, if this m-th BF wing crosses the k-th segment HF, the pressure differential between the i-th segment of SF and the wellbore can be expressed as follows:

$$\bar{m}_{wD}-\bar{m}_{SFD,i}=2\pi\left(\frac{S_{SF,i}^{BF,j}}{F_{CD,i}}+\frac{S_{BF,j}^{HF,k}}{F_{CD,j}}+\frac{S_{HF,k}^{W}}{F_{CD,k}}\right) \tag{33}$$

3.2.3 Coupling solution of MFHW

For the constant production rate of MFHW, the following forms of the production condition can be obtained:

$$\sum_{i=1}^{N_{t,FN}}\tilde{q}_{F,i}\Delta l_{s,i}=q_{sc} \tag{34}$$

where q_{sc} indicates the production condition, m^3/s; $\tilde{q}_{F,i}$ indicates the flow rate of i-th hyadrulic fracture element, m^3/s; $\Delta l_{s,i}$ indicates the length of i-th hydraulic fracture element, m.

Using the dimensionless parameter in Appendix A in Supplementary file and taking the Laplace transformation for Eq. (34), the following equation can be obtained:

$$\sum_{n=1}^{N_{t,FN}}\bar{\bar{q}}_{FD,n}\Delta l_{sD,n}=\frac{1}{s} \tag{35}$$

By combining Eqs. (21)-(22), Eqs. (28)-(37), and Eq. (35), a system of $N_{t,FN+1}$ linear equations was obtained. To facilitate the solution of the matrix, the following matrices were defined based on the relationship between the unknowns and equations:

(1) The column matrix of the dimensionless flow rate includes all the discrete HFN elements in the Laplace domain:

$$\begin{aligned}\mathbf{Q}_{fFD}=&[\underbrace{\bar{\bar{q}}_{fFD,1}\cdots\bar{\bar{q}}_{fFD,N_{t,HF}}}_{\text{all segments of HF}} \\ &\underbrace{\cdots\bar{\bar{q}}_{fFD,N_{t,BF}+N_{t,SF}}}_{\text{all segments of BF}}\underbrace{\cdots\bar{\bar{q}}_{fFD,N_{t,FN}}}_{\text{all segments of SF}}]^{\top}\end{aligned} \tag{36}$$

(2) The row matrix consists of the dimensionless length of all the discrete HFN elements:

$$\begin{aligned}&\mathbf{L}_{sD}= \\ &\left[\Delta l_{sD,1}\cdots\Delta l_{sD,N_{t,HF}}\cdots\Delta l_{sD,N_{t,HF}+N_{t,BF}}\cdots\Delta l_{sD,N_{t,FN}}\right]\end{aligned} \tag{37}$$

(3) The row matrix represents the length ratio of discrete segments for different types of discrete HFN elements:

$$\mathbf{R}_{s}=[\alpha_{i}]\,(i=1,2,\cdots N_{t,FN}) \tag{38}$$

where the α_i is as follows:

$$\alpha_{i}=\begin{cases}1,\ \text{for HF segments} \\ \dfrac{\Delta l_{sD,i}}{\Delta l_{sD,HF,n}},\ i\text{-th BF segments crossed with } n\text{-th HF segment} \\ \dfrac{\Delta l_{sD,i}}{\Delta l_{sD,BF,n}},\ i\text{-th SF segments crossed with } n\text{-th BF segment}\end{cases} \tag{39}$$

(4) The row matrix consists of the reciprocal conductivity of all hydraulic fractures multiplied by 2π:

$$\begin{aligned}\mathbf{F}_{CD}=&\left[\frac{2\pi}{F_{CD,1}}\cdots\frac{2\pi}{F_{CD,N_{t,HF}}}\cdots\frac{2\pi}{F_{CD,N_{t,HF}+N_{t,BF}}}\right. \\ &\left.\cdots\frac{2\pi}{F_{CD,N_{t,FN}}}\right]\end{aligned} \tag{40}$$

(5) The integral of the Bessel function in Eq. (24) can be expressed as the following matrix:

Table 2. Value of main parameters used for model validation sensitive analysis.

Parameter	Value	Parameters	Value
Reservoir thickness (m)	25.0	Matrix porosity (-)	0.06
Microfracture porosity (-)	0.005	HFN porosity (-)	0.002
Total matrix compressibility (Pa^{-1})	1.0×10^{-10}	Total microfracture compressibility (Pa^{-1})	1.5×10^{-10}
Total HFN compressibility (Pa^{-1})	2.0×10^{-10}	Matrix permeability (m^2)	1.0×10^{-19}
Microfracture permeability (m^2)	1.0×10^{-13}	Langmuir volume ($\mathrm{m}^3/\mathrm{m}^3$)	20.0
HF permeability (m^2)	4.0×10^{-12}	Langmuir pressure (MPa)	15.0
BF permeability (m^2)	2.0×10^{-12}	Reservoir temperature (K)	373.5
SF permeability (m^2)	1.0×10^{-12}	Initial reservoir pressure (MPa)	40.0
Horizontal well length (m^2)	240	Viscosity of gas at initial condition (Pa·s)	2.0×10^{-5}
Production condition (m^3/day)	2.0×10^4	Production test duration (day)	21.0

Table 3. Values of structural parameters of HFN.

Parameters	Value
Fracture height (m)	25.0
HF number (-)	2
BF number on single HF (-)	6
SF number on single HF (-)	8
HF discrete number (-)	16
BF discrete number (-)	6
SF discrete number (-)	12
HF half-length (m)	80
BF half-length (m)	15
SF half-length (m)	60

$$\begin{cases} \mathbf{M}_{SP} = [\beta_{i,j}] \quad (i = 1, 2, \cdots, N_{t,FN}; j = 1, 2, \cdots, N_{t,FN}) \\ \beta_{i,j} = \int_{\zeta_{mD,i}-\Delta l_{sD,i}/2}^{\zeta_{mD,i}+\Delta l_{sD,i}/2} \mathrm{K}_0 \left[r_D \sqrt{f_f(s)} \right] \mathrm{d}r_D \end{cases} \tag{41}$$

By substituting Eqs. (36)-(37) into Eq. (35), the following relationship could be obtained:

$$\mathbf{L}_{sD} \mathbf{Q}_{fFD} = \frac{1}{s} \tag{42}$$

To intersect the discrete HFN elements, their flow rate had to be added according to the supply relationship. The flow rate convergence can be represented as follows:

$$\mathbf{C}_{SB} \mathbf{C}_{BH} (\mathbf{R}_s \mathbf{E}) \mathbf{Q}_{fFD} = \mathbf{Q}_{FD} \tag{43}$$

where $\mathbf{C}_{SB}$ represents the rate connections of SF and BF segments; $\mathbf{C}_{BH}$ is the rate connections of BF and HF segments; and $\mathbf{E}$ is the element matrix, see Appendix C in Supplementary file for details.

Finally, taking Eqs. (36)-(43), these $N_{t,FN}$ + 1 equations can be rewritten as follows:

$$\begin{bmatrix} \mathbf{M}_{SP} + (\mathbf{E}\mathbf{F}_{CD}) \mathbf{D}_S & -\mathbf{I} \\ \mathbf{L}_{sD} (\mathbf{C}_{SB} \mathbf{C}_{BH} (\mathbf{R}_S \mathbf{E}))^{-1} & 0 \end{bmatrix} \begin{bmatrix} \mathbf{C}_{SB} \mathbf{C}_{BH} (\mathbf{R}_S \mathbf{E}) & \mathbf{O} \\ \mathbf{O}^{\mathrm{T}} & 1 \end{bmatrix} \begin{bmatrix} \mathbf{Q}_{fFD} \\ \bar{m}_{wD} \end{bmatrix} = \begin{bmatrix} \mathbf{O} \\ 1/s \end{bmatrix} \tag{44}$$

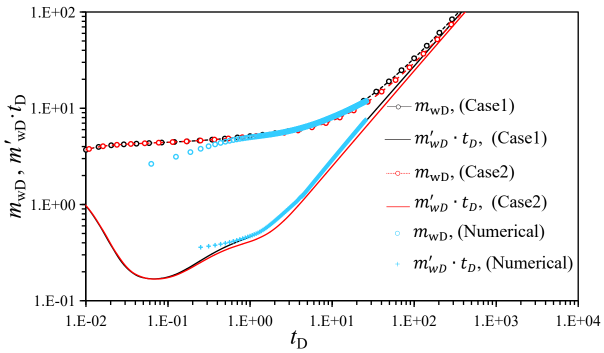

Fig. 7. Comparison of the numerical result with the type curve of Case 1 (our model) and Case 2 (the model ignores the IFNR and OFNR).

where **I** is the a column vector that all elements are 1; and **O** is a column vector that all elements are zero.

4. Results and discussion

The dimensionless pseudo-pressure of the wellbore, m_{wD}, was calculated in the Laplace domain using Eqs. (42)-(44). The Stehfest numerical inversion method was then applied to transform the solution from the Laplace space to the actual space. The value of the model's fundamental parameters is given in Table 2, and the value of the parameters related to the HFN structure is given in Table 3.

4.1 Model validation

The model was validated by conducting a numerical simulation using Petrel RE. The numerical simulation case was established with parameter values identical to those used in the model. The local grid refinement method was employed to generate the HFN spatially in the numerical model. The fracture grid width used in the numerical model was 0.025 m, with a maximum grid size of 0.5 m, and the grid height was set to DZ = 25 m. The value of hydraulic fracture parameters is given in Table 3.

Because to the use of an equal time step simulation in Petrel RE, the calculation of the initial production phase in t-

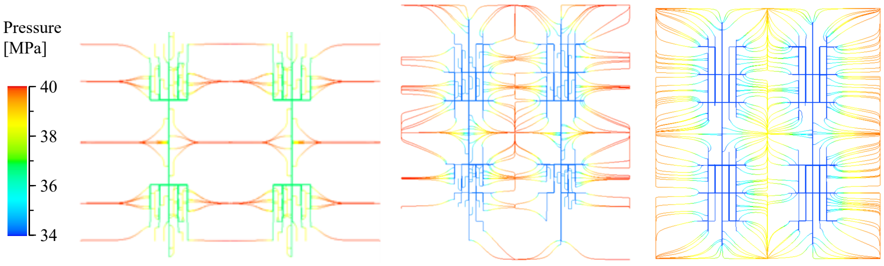

(a) (b) (c)

Fig. 8. The streamlines fields at different flow stages. (a) Early flow stage, (b) middle flow stage and (c) late flow stage.

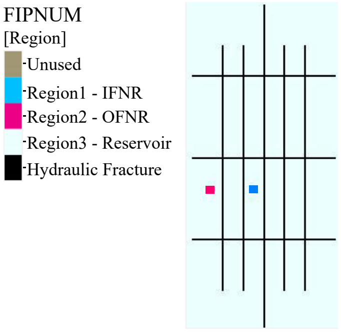

Fig. 9. Region division.

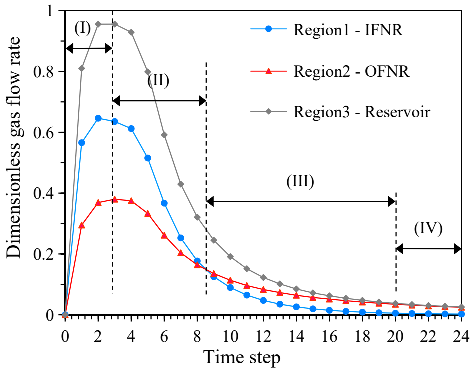

Fig. 10. Dimensionless gas flow rate of each FIP region at different simulation time steps.

he simulation results is less accurate than the well testing analysis. Consequently, the depiction of curve shapes for wellbore storage and the transition periods in the typical curve plot fall short of the desired level of accuracy. As shown in Fig. 7, however, as the simulation time increased, the numerical simulation results could be well fitted to the proposed model when it reached the middle flow period, which proved the correctness of our model.

Furthermore, to enhance the understanding of flow distribution characteristics at various flow stages in the MHFW model with HFN, streamline fields from the simulator outputs were utilized to visualize the flow patterns during different production stages. As shown in Fig. 8(a), the streamline was developed mainly in the HFN, and the neighboring matrix was in the early flow stage. As production time progressed, the area of pressure drops propagated gradually, as shown in Fig. 8(b), along the distribution of the streamline not only in HFN but also in the IFNR and OFNR. This propagation indicated that the fluid of the matrix system fed to the HFN. At a later stage of production, as shown in Fig. 8(c), the streamline existed only in the HFN and OFNR but not in the IFNR. This phenomenon was consistent with that envisagement in our model that no fluid was supplied from OFNR to the IFNR and that the pressure systems of IFNR and OFNR were discontinuous.

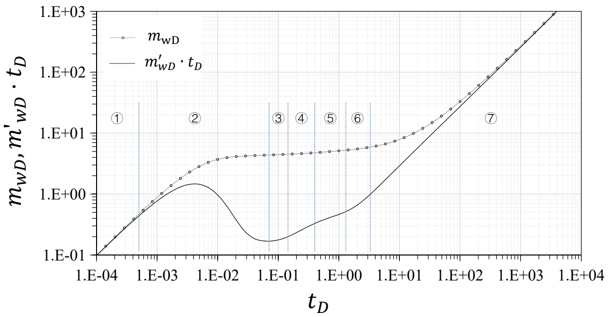

Fig. 11. Typical curve with flow stage dividing.

To quantitatively analyze the regularity of the gas flow rate change at different flow stages between IFNR and OFNR, the previous numerical simulation example used the keyword FIPNUM (fluid-in-place numbers). The simulation selected the regions with the same areas in IFNR and OFNR and gave a differentiated FIP-region index, as shown in Fig. 9. The flow transmission relationship between each FIP region was determined based on the numerical simulator results. The curve depicting the flow transmission relationship versus the simulation time steps for each FIP region was plotted, as shown in Fig. 10. Four distinct regimes were observed as follows: Section I reflected the process of continuous establishment of the pressure drop at the initial flow stage, and in this regime, the flow rate of Region 1 was higher than that of Region 2. In section II, the flow in each FIP region began to decrease. Because the density of HFN around Region 1 was greater than Region 2, the flow rate of Region 1 decreased faster than Region 2. Finally, the flow rate of Region 1 was equal to that of Region 2. At the beginning of section III, the flow rate of Region 1 was lower than Region 2, and the flow rate in Region 1 finally tended toward zero because of the lack of fluid supply. In section IV, the flow rate of Region 3 was equal to Region 2, which indicated that fluid did not pass thr-

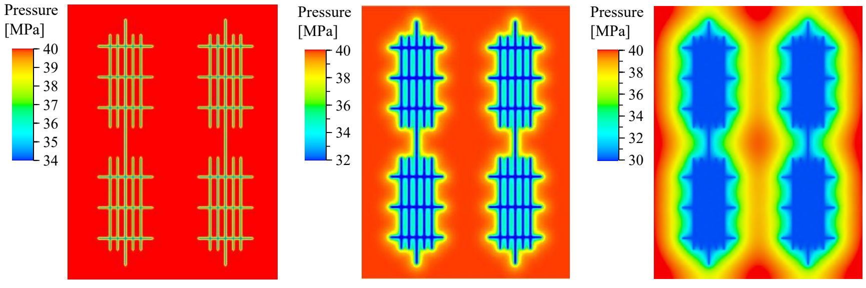

(a) (b) (c)

Fig. 12. Pressure distribution at different flow stages. (a) Bilinear flow, (b) formation linear flow and (c) biradial flow.

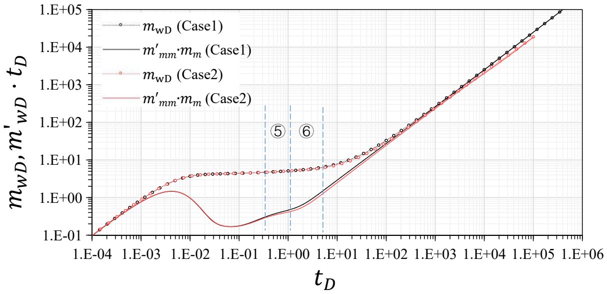

Fig. 13. Comparison of the typical curves for Case1 and Case2.

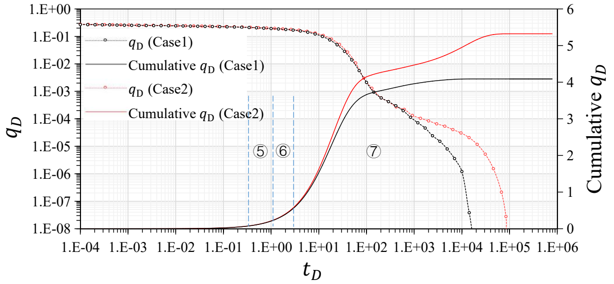

Fig. 14. Comparison of dimensionless production rate q_D and dimensionless cumulative gas production rate for Case1 and Case2.

ough Region 1. Therefore, by quantitatively describing the variation of the flow rate in IFNR and OFNR, it is proved that the difference between IFNR and OFNR envisaged by the seepage model proposed in this study is correct.

4.2 Typical curve and discussion

The typical curves for the model calculation results are depicted in Fig. 11. Based on the shape characteristic and slope of the derivative curve, the entire curve was divided into multiple flow stages. The division of flow stages has been extensively discussed and comprehended in previous studies (Agarwal et al., 1970; Cinco-Ley and Samaniego, 1981; Tiab, 1993; Kuchuk et al., 2010; Chen et al., 2018). Based on this insights, the flow stages of the typical curves for the proposed model were divided as follows:

Stage 1 is the wellbore storage stage. The Laplace variable s tends toward infinity during this stage, and the pseudo-pressure and its derivative curve are a straight line with a unit slope. The solution of bottom-hole pressure reflects the influence of the wellbore storage coefficient (Chen et al., 2018). Stage 2 is the early transitional stage. The pseudo-pressure derivative curve has the obvious form of rising and falling in this stage, reflecting the flow choking that occurs between the HFN and wellbore (Agarwal et al., 1970; Cinco-Ley and Samaniego, 1981; Tiab, 1993; Kuchuk et al., 2010; Chen et al., 2018). Stage 3 is the bilinear flow stage with the unique feature that the slope of the $m'_{wD} - t_D$ curve in the typical log-log plot equals 0.25 (Cinco-Ley and Samaniego, 1981; Chen et al., 2018). This stage reflects the appearance of pressure differences in microfractures, and the simultaneous flow of fluid in the HFN and the microfractures occurs. The pressure distribution caused by the fluid produced at this stage is shown in Fig. 12(a). Stage 4 is the formation flow stage. The curve of the dimensionless pseudo-pressure derivate versus dimensionless time in the typical curve has the 1/2 slope. This flow stage shows the pressure difference in a broader range of microfractures that are formed (Cinco-Ley and Samaniego, 1981). The pressure distribution is shown in Fig. 12(b). Stage 5, which is commonly called the biradial flow stage, has the feature that the $m'_{wD} - t_D$ curve is a straight line with a slope of approximately 1/3 (Tiab, 1993). This flow stage reflects that the front of the pressure difference has reached the area outside the HFN (Chen et al., 2018), which can be seen in the pressure distribution diagram shown in Fig. 12(c). Stage 6 has the particular characteristic that the shape of the pseudo-pressure derivative curve in the typical curve has gradually flattened after the bi-radial flow stage and its subsequent dramatic increase. This change reflects the fact that the propagation of pressure drop has reached a brief stable stage. Stage 7 is the boundary control flow stage. In this stage, the shape of pseudo-pressure and its derivative curve overlaps, and the unit slope of the seepage model is assumed to be the closed outer boundary of the reservoir.

To illustrate the significance of the characteristics considered in the model, a comparison was made between the typical curves of transient pressure response (depicted in Fig. 13) and production rate (depicted in Fig. 14) for two cases: Case 1 is our model, and Case 2 is the model showing that the outer seepage boundary of the shale matrix in the IFNR is the same as that of the OFNR. As shown in Fig. 13, the shapes of the pseudo-pressure derivative curves of Case1 (our model) and Case 2 (the model ignores the IFNR and OFNR) are different.

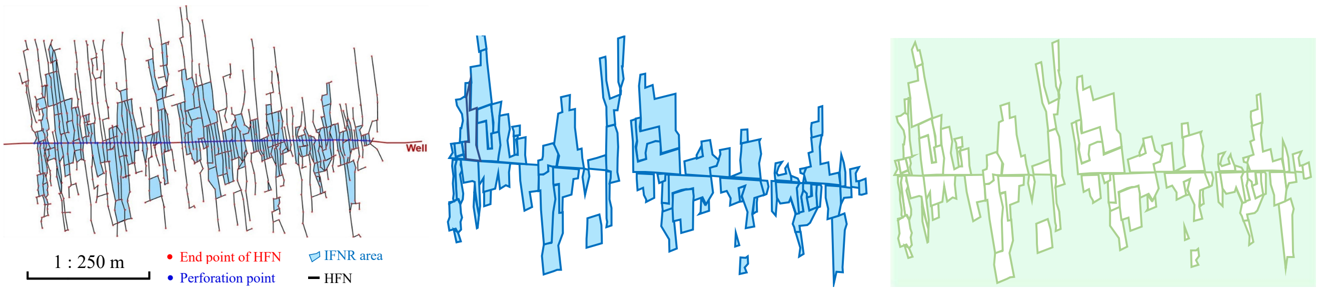

(a) (b) (c)

Fig. 15. Model of the field case. (a) HFN generated by fracturing simulation, (b) IFNR area and (c) OFNR area.

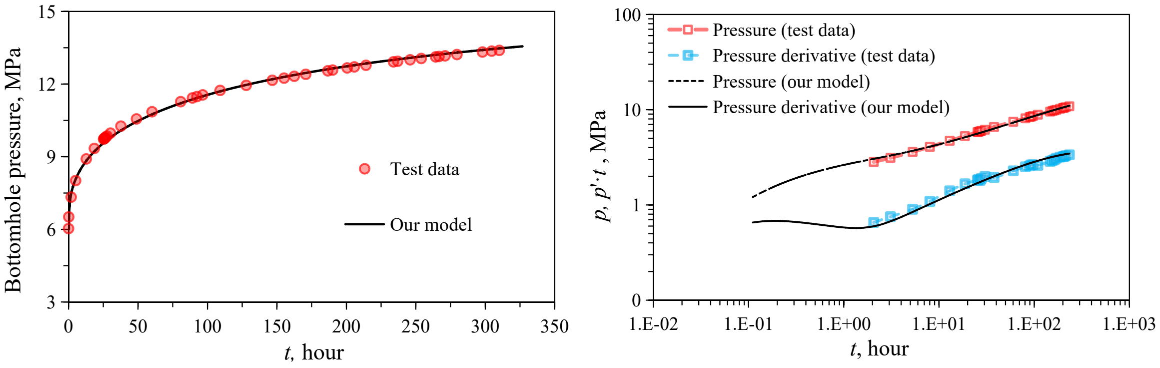

(a) (b)

Fig. 16. Curves of the bottomhole pressure matching. (a) Bottom hole pressure fitting and (b) PTA type curves fitting.

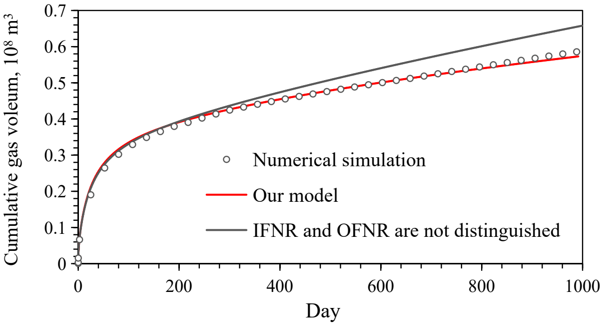

Fig. 17. Production forecast comparison with various models.

From the start of the biradial flow stage, the curve position of Case 1 was higher than that of Case 2. Because there is no external fluid supply in the IFNR matrix, this indicated that in Case 1 a higher production pressure difference was required to meet the production condition of MFHW. Another difference between the typical curves of Case 1 and Case 2 is that the boundary control flow stage occurred earlier. The production difference between Case 1 and Case 2 is shown in Fig. 14. The gas production rate and cumulative gas production of Case 1 were lower than that of Case 2. The EUR obtained by our model was approximately 27.0% lower than that of the model that ignored the difference in the outer seepage boundary between the matrix system of the IFNR and the OFNR.

4.3 Field application

In addition to traditional well testing analysis, the proposed model can be used in conjunction with the hydraulic fracture simulation results to perform a dynamic analysis and prediction of gas wells. Fig. 15(a) shows the hydraulic fracturing simulation results of an actual test well, revealing a clear network structure of hydraulic fractures. On the basis of the methodology of this study, the modified area is first divided into the IFNR and OFNR regions, as shown in Figs. 15(b) and 15(c). Using Eqs. (2)-(3), the area of each IFNR and the corresponding FCR area could be calculated. This calculation allows for the determination of the boundary for each FCR region, which is then incorporated into the flow model.

Furthermore, it is well known that due to the multi-solution of the PTA, the type curve fitting may be achieved by using different PTA models, but the parameters inversion result will be different. Fig. 17 illustrates the comparison of the production forecasts for the given case using various models. It can be observed that our model closely aligns with the numerical simulation, whereas the production forecasts exhibit a significant increase of approximately 23.6% when the distinction between IFNR and OFNR is not considered.

5. Conclusions

1) According to the streamline output by numerical simulation, in the later stage of production, the streamline was distributed only in the OFNR, whereas the IFNR was not

streamlined. In addition, the decline of the gas flow rate of the IFNR was more rapid than that of the OFNR. The gas well production came only from the OFNR in the later flow stage, which indicated that it was necessary to consider differences in the supply boundaries between the IFNR and the OFNR.

2) If the seepage model of the MFHW with HFN ignored the difference in the flow boundary between the IFNR and the OFNR, the EUR would be overestimated, and the stage of boundary control flow would appear later.
3) The typical curve of our model could be divided into 7 flow stages as follows: Wellbore storage stage, early transitional stage, bilinear flow stage, formation flow stage, biradial flow stage, later transition flow stage, and boundary control stage.
4) The dimensionless conductivity of hydraulic fracture is a parameter group that is jointly determined by the width, length, and permeability of hydraulic fractures and the permeability of microfracture. Thus, it was better to analyze the model parameter individually instead of applying the parameter group, such as only in PTA.

Acknowledgements

National Science Fund for Excellent Young Scholars (No. 52222402), Sichuan Science and Technology Program (No. 2022JDJQ0009), Science and Technology Cooperation Project of the CNPC-SWPU Innovation Alliance (Nos. 2020CX020202, 2020CX030202 and 2020CX010403).

Supplementary file

https://doi.org/10.46690/ager.2023.06.06

Conflict of interest

The authors declare no competing interest.

References

Afagwu, C., Abubakar, I., Kalam, S., et al. Pressure-transient analysis in shale gas reservoirs: A review. Journal of Natural Gas Science and Engineering, 2020, 78: 103319.

Agarwal, R. G., Al-Hussainy, R., Ramey, H. J. An investigation of wellbore storage and skin effect in unsteady liquid flow: I. Analytical treatment. SPE Journal, 1970, 10(3): 279-290.

Brown, M., Ozkan, E., Raghavan, R., et al. Practical solutions for pressure-transient responses of fractured horizontal wells in unconventional shale reservoirs. SPE Reservoir Evaluation & Engineering, 2011, 14(6): 663-676.

Chen, Z., Liao, X., Sepehrnoori, K., et al. A semi-analytical model for pressure transient analysis of fractured wells in unconventional plays with arbitrarily distributed fracture networks. Paper 187290 Presented at SPE Annual Technical Conference and Exhibition, San Antonio, Texas, 9-11 October, 2017.

Chen, Z., Liao, X., Yu, W., et al. Pressure-transient behaviors of wells in fractured reservoirs with natural and hydraulic-fracture networks. SPE Journal, 2018, 24(1): 375-394.

Chu, H., Zhang, J., Zhang, L., et al. A new semi-analytical flow model for multi-branch well testing in natural gas hydrates. Advances in Geo-energy Research, 2023, 7(3): 176-188.

Cinco-Ley, H., Samaniego, V. F. Transient pressure analysis for fractured wells. Journal of Petroleum Technology, 1981, 33(9): 1749-1766.

Cipolla, C. L., Lolon, E. P., Erdle, J. C., et al. Reservoir modeling in shale-gas reservoirs. SPE Reservoir Evaluation & Engineering, 2010, 13(4): 638-653.

Clarkson, C. R., Nobakht, M., Kaviani, D., et al. Production analysis of tight-gas and shale-gas reservoirs using the dynamic-slippage concept. SPE Journal, 2012, 17(1): 230-242.

Daniels, J. L., Waters, G. A., Calvez, J. H. L., et al. Contacting more of the Barnett Shale through an integration of real-time microseismic monitoring, petrophysics, and hydraulic fracture design. Paper SPE 110562 Presented at SPE Annual Technical Conference and Exhibition, Anaheim, California, 11-14 November, 2007.

El-Banbi, A. H., Wattenbarger, R. A. Analysis of linear flow in gas well production. Paper SPE 39972 Presented at SPE Gas Technology Symposium, Calgary, Alberta, 15-18 March, 1998.

Ertekin, T., King, G. R., Schwerer, F. C. Dynamic gas slippage: A unique dual mechanism approach to the flow of gas in tight formations. SPE Formation Evaluation, 1986, 1(1): 43-52.

Fan, D., Ettehadtavakkol, A. Analytical model of gas transport in heterogeneous hydraulically-fractured organic-rich shale media. Fuel, 2017, 207: 625-640.

Fisher, M. K., Wright, C. A., Davidson, B. M., et al. Integrating fracture mapping technologies to optimize stimulations in the Barnett Shale. Paper SPE 77441 Presented at SPE Annual Technical Conference and Exhibition, San Antonio, Texas, September 29-October 2, 2002.

Gringarten, A. C., Ramey, Jr H. J. The use of source and Green's Functions in solving unsteady-flow problems in reservoirs. SPE Journal, 1973, 13(5): 285-296.

Hazlett, R. D., Farooq, U., Babu, D. K. A complement to decline curve analysis. SPE Journal, 2021, 26(4): 2468-2478.

Holditch, S. A. The increasing role of unconventional reservoirs in the future of the oil and gas business. Journal of Petroleum Technology, 2003, 55(11): 34-79.

Jia, P., Cheng, L., Huang, S., et al. Transient behavior of complex fracture networks. Journal of Petroleum Science and Engineering, 2015, 132: 1-17.

Jia, P., Cheng, L., Huang, S., et al. A comprehensive model combining Laplace-transform finite-difference and boundary-element method for the flow behavior of a two-zone system with discrete fracture network. Journal of Hydrology, 2017, 551: 453-469.

Karimi-Fard, M., Durlofsky, L. J., Aziz, K. An efficient discrete-fracture model applicable for general-purpose reservoir simulators. SPE Journal, 2004, 9(2): 227-236.

Kuchuk, F., Onur, M., Hollaender, F. Pressure transient formation and well testing: Convolution, deconvolution, and nonlinear estimation, in Developments in Petroleum Science, Elsevier. edited by F. Kuchuk, F. Hollaender, M. Onur, Elsevier, Amsterdam, pp, 1-389, 2010.

Miao, F., Wu, D., Liu, X., et al. Methane adsorption on shale under in situ conditions: Gas-in-place estimation considering in situ stress. Fuel, 2022, 308: 121991.

Moghanloo, R. G., Javadpour, F. Applying method of characteristics to determine pressure distribution in 1D shale-gas samples. SPE Journal, 2014, 19(3): 361-372.

Nguyen, K. H., Zhang, M., Ayala, L. F. Transient pressure behavior for unconventional gas wells with finite-conductivity fractures. Fuel, 2020, 266: 117119.

Ozkan, E., Brown, M., Raghavan, R., et al. Comparison of fractured horizontal-well performance in conventional and unconventional reservoirs. Paper SPE 121290 Presented at SPE Western Regional Meeting, San Jose, California, 24-26 March, 2009.

Ozkan, E., Raghavan, R., Apaydin, O. G. Modeling of fluid transfer from shale matrix to fracture network. Paper SPE 134830 Presented at SPE Annual Technical Conference and Exhibition, Florence, Italy, 19-22 September, 2010.

Palmer, I. Modeling shear failure and stimulation of the Barnett Shale after hydraulic fracturing. Paper SPE 106113 Presented at SPE Hydraulic Fracturing Technology Conference, College Station, Texas, 29-31 January, 2007.

Ren, Z., Yan, R., Huang, X., et al. The transient pressure behavior model of multiple horizontal wells with complex fracture networks in tight oil reservoir. Journal of Petroleum Science and Engineering, 2019, 137: 650-665.

Stalgorova, E., Matter, L. Analytical model for unconventional multi-fractured composite systems. SPE Reservoir Evaluation & Engineering, 2013, 16(3): 246-256.

Tiab, D. Analysis of pressure and pressure derivative without type-curve matching-III. Vertically fractured wells in closed systems. Paper SPE 26138 Presented at the SPE Western Regional Meeting, Anchorage, Alaska, 26-28 May, 1993.

Tian, S., Wang, T., Li, G., et al. An analytical model for shale gas transport in circular tube pores. International Journal of Heat and Mass Transfer, 2018, 127: 321-328.

Waltman, C. Comparison of single and dual array microseismic mapping techniques in the Barnett Shale. Paper SPE 95568 Presented at SPE Annual Technical Conference and Exhibition, Dallas, Texas, 6-11 November, 2005.

Wang, H. Performance of multiple fractured horizontal wells in shale gas reservoirs with consideration of multiple mechanisms. Journal of Hydrology, 2014, 510: 299-312.

Wang, H., Chen, L., Qu, Z., et al. Modeling of multi-scale transport phenomena in shale gas production - A critical review. Applied Energy, 2020, 262: 114575.

Wang, W., Fan, D., Sheng, G. A review of analytical and semi-analytical fluid flow models for ultra-tight hydrocarbon reservoirs. Fuel, 2019, 256: 115737.

Wang, T., Tian, S., Zhang, W., et al. Production model of a fractured horizontal well in shale gas reservoirs. Energy & Fuels, 2021, 35(1): 493-500.

Wattenbarger, R. A., El-Banbi, A. H., Villegas, M. E., et al. Production analysis of linear flow into fractured tight gas wells. Paper SPE 39931 Presented at the SPE Rocky Mountain Regional/Low-Permeability Reservoirs Symposium, Denver, Colorado, 5-8 April, 1998.

Yao, S., Zeng, F., Liu, H., et al. A semi-analytical model for multi-stage fractured horizontal wells. Journal of Hydrology, 2013, 507: 201-212.

Zhang, R., Chen, M., Zhao, Y., et al. Production performance simulation of the fractured horizontal well considering reservoir and wellbore coupled flow in shale gas reservoirs. Energy & Fuels, 2022, 36(22): 13637-13651.

Zhang, Y., Yang, D. Modeling transient pressure behavior of a multi-fractured horizontal well in a reservoir with an arbitrary boundary and different fracture networks by considering stress-sensitive effect. Journal of Hydrology, 2021, 600: 126552.

Zhao, K., Du, P. Performance of horizontal wells in composite tight gas reservoirs considering stress sensitivity. Advances in Geo-Energy Research, 2019, 3(3): 287-303.

Zhao, Y., Li, H., Zhang, L., et al. Pressure transient analysis for off-centered fractured vertical wells in arbitrarily shaped gas reservoirs with the BEM. Journal of Petroleum Science and Engineering, 2017, 156: 167-180.

Zhao, Y., Zhang, L., Xiong, Y., et al. Pressure response and production performance for multi-fractured horizontal wells with complex seepage mechanism in box-shaped shale gas reservoir. Journal of Natural Gas Science and Engineering, 2016, 32: 66-80.

Zhao, Y., Zhang, L., Zhao, J., et al. Performance of fractured horizontal well with stimulated reservoir volume in unconventional gas reservoir. Journal of Hydrology, 2014, 512: 447-456.